Contents lists available at Egyptian Knowledge Bank

Labyrinth: Fayoum Journal of Science and Interdisciplinary Studies

Journal homepage: https://lfjsis.journals.ekb.eg/

Thermal and dielectric properties of disordered rocksalt Li-excess $Li_{1.3}Nb_{0.3}Mn_{0.4}O_2$ cathode material for lithium-ion batteries

Mohamed Kamel [a], Mahmoud Abdel-Hafiez [a, b], Abdelwahab Hassan [a], Arafa Hassen [a,*]

[a] *Physics Department, Faculty of Science, Fayoum University, El Fayoum 63514, Egypt.*
[b] *Department of Physics and Astronomy, Uppsala University, 75120 Uppsala, Sweden.*

ARTICLE INFO

Keywords:
Lithium-ion batteries $Li_{1.3}Nb_{0.3}Mn_{0.4}O_2$
Thermal Analyses
Dielectric Properties

ABSTRACT

As one of the remarkable cathode materials for lithium-ion batteries, the disordered rocksalt Li-excess $Li_{1.3}Nb_{0.3}Mn_{0.4}O_2$ (LNMO) revealed attractive behaviors. Herein, Fourier transform infrared (FTIR) spectroscopy, thermogravimetric analysis (TGA), and differential scanning calorimetry (DSC) for the as-prepared LNMO were reported. The symmetrical bending and stretching vibrations of Li-O and Mn-O appeared in the range 480-700 cm^{-1}. The reaction enthalpy (ΔH) is found to be 306.78 J/g. The dielectric properties were also studied at various frequencies and temperatures. At low frequencies, the LNMO has high permittivity as well as losses. The AC conductivity and the dielectric modulus at various frequencies and temperatures were also discussed. Different dielectric parameters were given for the LNMO sample. All general outcome results of LNFO emphasize the importance of such lithium-ion battery cathode material in the applications.

1. Introduction

Within the past few decades, the demands for sources of energy storage satisfying high performance as well as safety have increased. Rechargeable lithium-ion batteries (LIBs) are among these sources that are characterized by remarkable features, such as high capacity, working voltage, safety, and large cycle period [1-5]. Remarkably, there is an energy gap between the cathode and the anode materials that LIBs performance is restricted by the energy densities associated with cathode materials [6, 7]. A huge number of attempts have been done to synthesize cathode materials to provide high energy density with several factors being taken into the cost [8-10].

Among the recently revealed cathode materials, the cation-disordered rocksalt Li-excess (DRX) cathode materials have an intense attraction due to their characteristics [11-14]. The DRX cathode materials can deliver energy densities over about 1000 (Wh/kg) [15]. Urban et al. [16] reported a considerable cation disordering and Li excess in the rocksalt structure (NaCl-structure) lead to DRX materials that can produce high capacities compared to other commercial materials [16]. The cation disordering which means the random distribution of Li and transition metal (TM) at the cation sublattice 4a sites creates zero-TM channels. Such channels have no TMs in the face-sharing octahedra and act as the main channel for Li diffusion [16-18]. It is suggested that the existence of the d0 transition metal is vital for creating disordered rocksalt phases [17].

In 2015, Yabuuchi et al. [19] reported the niobium-based high-capacity cathode material, $Li_{1.3}Nb_{0.3}Mn_{0.4}O_2$ that delivers high noticeable reversible capacities up to 300 $mAh.g^{-1}$. The output high capacity refers to applying a Mn^{2+}/Mn^{4+} redox couple that utilizes a redox reaction of two electrons ($2e^-$) [12, 19]. Recently, Kamel et al. [20] reported the optical, magnetic, and thermodynamic properties of this compound.

Since most studies are directed toward electrochemistry performance, there are few concerning fundamental studies such as thermal and dielectric properties. Furthermore, the thermal analysis for cathode materials of LIBs is very important to understand their behavior at elevated temperatures [21]. This work aimed to throw light on the thermal analysis up to 995 °C, FTIR spectra, and the electrical properties of LNMO at different temperatures as well as different frequencies.

* Corresponding author.
E-mail address: ash02@fayoum.edu.eg (A. Hassen); Tel.: +201001104150
DOI: 10.21608/ifjsis.2023.296457
Received 10 March 2023; Received in revised form 8 April 2023; Accepted 8 April 2023
Available online 26 April 2023

2. Experimental part

2.1. Synthesis

The synthesis of the LNMO was previously reported [20, 22]. For the dielectric measurements, the as-prepared LNMO powder sample is pressed using a hydraulic press at about 3 tons into a round pellet of diameter and thickness of 1 cm and 2.7 mm, respectively. The pellet is then sintered at 950 °C for 12 h in an argon atmosphere. Then, the two round sides of the pellet were coated with silver paste.

2.2. Characterization

The attenuated total reflectance Fourier Transform Infrared (ATR-FTIR) spectrum was collected on an Invenio-R FTIR spectrometer (Bruker). The measurements were performed using a Bruker Platinum ATR with a diamond crystal. The thermogravimetric analysis (TGA), and differential scanning calorimetry (DSC) data were obtained using Simultaneous Thermal Analyzer (STA) 6000 (PerkinElmer) in a range of temperatures ranging from 303 to 1268 K in a nitrogen atmosphere, and a heating rate of 10 °C/min. The dielectric properties were measured at different temperatures by using the LCR meter (Hioki IM 3536) in a frequency range from 100 Hz to 8 MHz with an accuracy of ± 1 × 10^{-4} pF.

3. Results and discussion

3.1. Characterization

The structure of the polycrystalline LNMO sample has a disordered structure with the space group *Fm-3m* (number 225) as reported previously by Kamel et al. [20]. Fig. 1 illustrates the FTIR spectrum of the LNMO sample in the wavenumber range of 400-4000 cm^{-1}. Table 1 summarizes the main peaks at different wavenumbers.

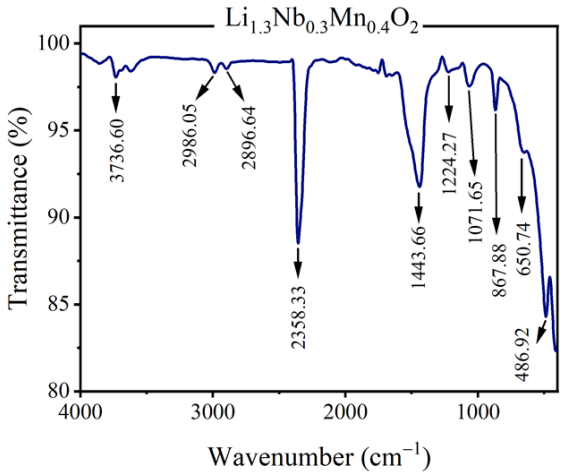

Fig. 1. FTIR spectrum of $Li_{1.3}Nb_{0.3}Mn_{0.4}O_2$.

The symmetrical bending and stretching vibrations of Li-O and Mn-O, and Nb-O appear in the wavenumber range of 480 and 700 cm^{-1} [23-26]. The peaks (867, 1071, and 1224 cm^{-1}) are attributed to the Li_2CO_3 impurity released from the reaction between unreacted carbon dioxide and Li salt on the surface of Li-excess particles [27, 28]. The bands 1443 and 3736 refer to the O-H stretching vibrations, and the bands 2358, 2896, and 2986 cm^{-1} can be assigned to the C-H stretching vibrations [29].

Table 1: The FTIR mean peaks and corresponding assignments for $Li_{1.3}Nb_{0.3}Mn_{0.4}O_2$

Wavenumber (cm^{-1})	Assignments
480	Li-O and Mn-O, and Nb-O bending and stretching vibrations [23-26]
700	Li-O and Mn-O, and Nb-O bending and stretching vibrations
867	Li_2CO_3 impurity [27, 28]
1071	Li_2CO_3 impurity
1224	Li_2CO_3 impurity
1443	O-H stretching vibrations [29]
2358	C-H stretching vibrations [29]
2896	C-H stretching vibrations
2986	C-H stretching vibrations
3736	O-H stretching vibrations

3.2. *Thermal analysis*

The thermogravimetric analysis (TGA), derivative thermogravimetric (DTG), differential scanning calorimetry (DSC), and the specific heat (C_p) of the LNMO sample are shown in Fig. 2(a-d). One noted that the TGA curve (Fig. 2(a)) can be divided into different loss parts. The first part started to decompose at room temperature due to the heating-up process leading to the evaporation of water molecules in the compound [30-32]. The weight is continued to decrease with increasing temperature. The weight loss is estimated to be 4.81 %. at 613 K. Another weight loss is 5.16 % at 789 K and occurred with further increasing temperature owing to the decrease in the density of the compound. A sudden increase in the weight that occurred from 802 to 895 K could be attributed to some oxides being released. This sudden increase or weight gain (0.7 %) is due to the oxidation process. Finally, the last weight loss (2.37 %) appeared at 1004 K to 1100 K, and then the weight was almost stable at high temperatures up to 1264 K. Fig. 2(b) indicates the derivative of the weight (DTG) to demonstrate the weight losses.

Besides, the DSC curve (Fig. 2(c)) showed a weak endothermic peak around 1055 K, where the reaction enthalpy (ΔH) was calculated to be 306.78 J/g. This indicates the thermal stability of the LNMO sample. Fig. 2(d) depicts the specific heat (C_p) as a function of the temperature. The initial temperature (T_i) of the reaction is found to be 1020 K, and the specific heat corresponding to this temperature is 5.44 kJ/mol K. Also, the end of this reaction or the final temperature (T_f) is 1105 K and C_p = 3.13 kJ/mol K. This observed peak in the DSC and associated specific heat curve may be due to the change of the oxidation state in the LNMO compound [33, 34].

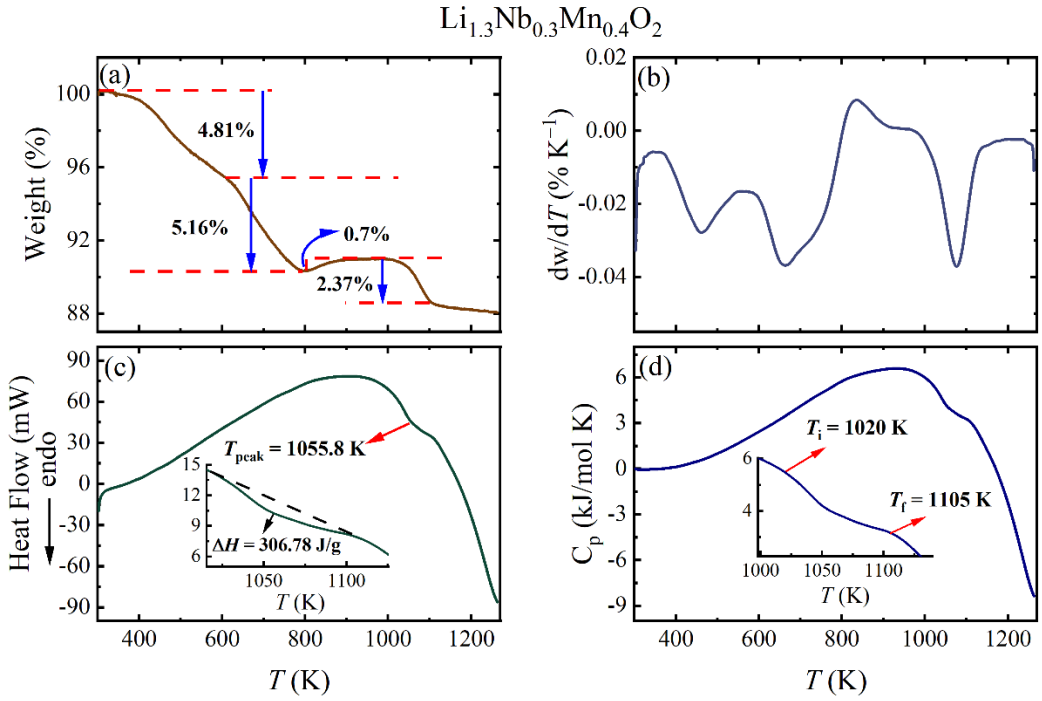

Fig. 2. (a) Thermogravimetric analysis (TGA); (b) the derivative thermogravimetric (DTG); (c) differential scanning calorimetry (DSC) (heat flow endo down). The inset in (c) indicates such a weak endothermic peak for the reaction; (d) the specific heat C_p against the temperature. The inset in (d) illustrates the initial temperature for the reaction T_i and the final temperature T_f for $Li_{1.3}Nb_{0.3}Mn_{0.4}O_2$.

3.3. *Dielectric properties*

Frequency dependence

The dielectric measurements are considered a potent tool to study the dynamic properties of the sample such as conductance, permittivity, and loss factor [35, 36]. Through the dielectric properties, we can obtain some information about the grain and grain boundaries of the studied compound and its structure [37]. The complex permittivity (ε^*) as well as the dielectric loss tangent (tan δ) of a substance is described as [38, 39]:

$$\varepsilon^* = \varepsilon' - i\varepsilon'' \quad (1)$$

$$tan\,\delta = \varepsilon''/\varepsilon' \quad (2)$$

where ε', ε'' are the real (dielectric constant) and imaginary parts of complex permittivity. The dielectric loss is associated with the energy loss and takes place in case there are shifts of the polarization behind the applied electric field owing to the grain boundaries [37]. There are three featured factors responsible for the dielectric loss of the materials: (i) space charge migration, (ii) direct current conduction, and (iii) dipole loss or the molecular dipoles movement [40]. Fig. 3 (a-d) presents ε', ε'', tan δ and AC conductivity (σ_{AC}) against the frequency (f) at different temperatures. Regarding ε' against log f plot (Fig. 3(a)), ε' deceases with increasing the frequency and its value became constant at high frequencies. This behavior is similar for ε''

against log f (Fig. 3(b)). On the other hand, the change of dielectric loss tangent (tan δ) with the frequency (Fig. 3(c)) showed that tan δ decreases as the frequency increases. Then, it slightly increases and exhibits a broad peak. It is noticed that the peak shifts as the temperature raised which gives evidence for the temperature dependence of tan δ. The high values of ε', ε'', and tan δ in the low frequencies range refer to the accumulations of the space charge polarization [39]. Such high values at low frequencies are related to Li^+ ions at the electrode interface and increased polarization in addition to the high resistivity of grain boundaries compared to the grains [37, 39]. However, according to Jonscher's universal power law, the $\sigma_{AC}(f)$ is expressed according to Jonscher's universal power law [41]:

$$\sigma_{AC}(f) = \sigma_{t-}\sigma_{DC} \approx Af^m \quad (3)$$

where σ_{DC} is the σ_{AC} at $f \to 0$, A is a constant that depends on temperature, σ_t is the total conductivity, and m is known as the frequency exponent. The frequency dependence of σ_{AC} at different temperatures is illustrated in Fig. 3(d). There is an obvious gradual increase of σ_{AC} as the frequency increases. The σ_{AC} curves at various temperatures merge to one single curve at high frequencies region (f > 6 MHz).

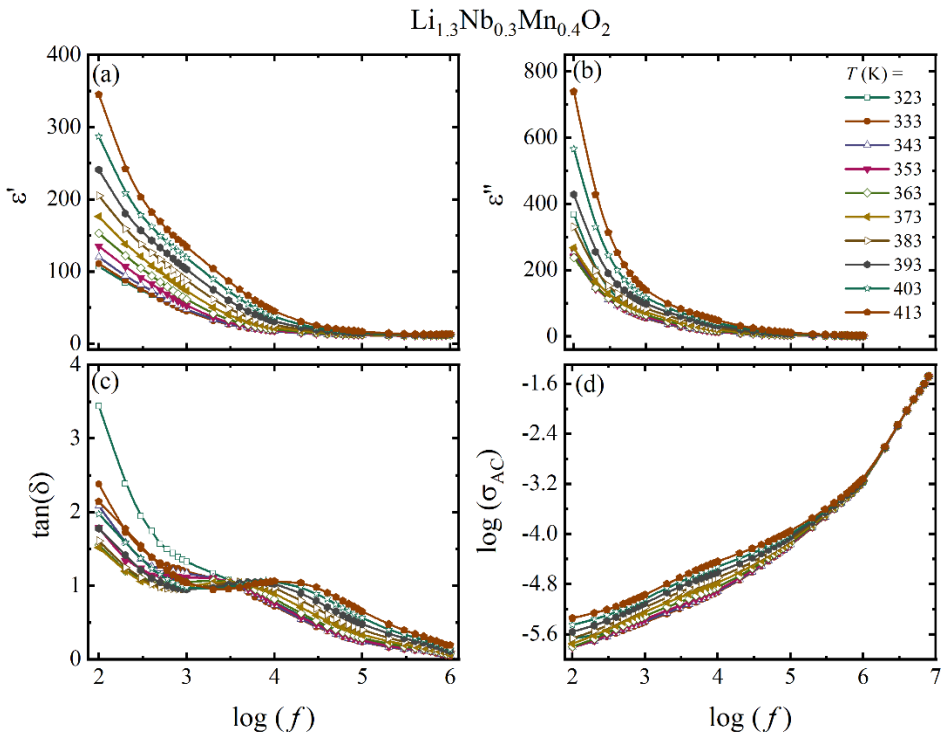

Fig. 3. The variation of (a) dielectric constant (ε'); (b) dielectric loss (ε''); (c) the loss factor (tan δ); (d) log σ_{AC} with log f at various temperatures.

For further understanding of the conduction mechanism of LNMO sample, Fig. 4(a) displays log σ_{AC} against the angular frequency, log (ω), at various temperatures. As ω increases, σ_{AC} has a linear increase. Jonscher's power law (Eq. 3) was used to fit the data. Table 2 listed the frequency exponent (m) at different temperatures. As shown in Table 2, the values of m are located between 0 and 1. Hence, the conduction mechanism is associated with the correlated barrier hopping (CBH) model [42-44]. In this model as the temperature increases the frequency exponent (m) decreases, and (m) is descibed as [45-47]:

$$m(T) = 1 - \frac{6k_BT}{W_M + k_BT\ ln(\omega\tau_0)} \quad (4)$$

where W_M is the required binding energy to transfer a charge carrier from one site to another, τ_0 denotes the characteristic relaxation time, and k_B is Boltzmann constant. In the case that $W_M \gg k_BT\ \ln(\omega\tau_0)$, Eq. 4 can be written as:

$$m(T) = 1 - \frac{6k_BT}{W_M} \quad (5)$$

Fig. 4(b) illustrates the temperature dependence of the frequency exponent ($m - 1$). From the fitting using equation (5), the average binding energy W_M is calculated to be 201 meV.

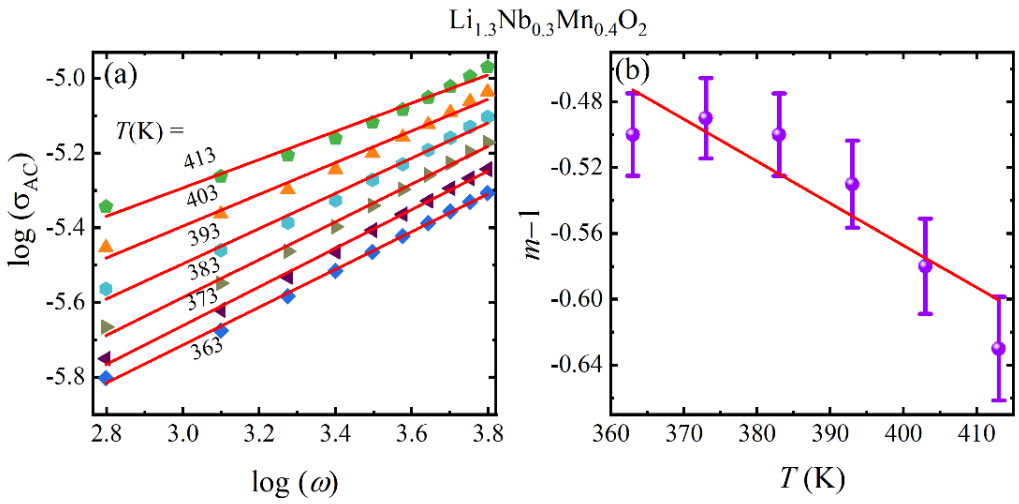

Fig. 4. (a) The variation of log σ_{AC} versus log ω at various temperatures. The red lines demonstrate the linear fitting according to Eq. 3; (b) temperature dependence of frequency exponent (m-1). The red line indicates the linear fitting using Eq. 5.

Table 2. The frequency exponent (m) at different temperatures.

T (K)	M
363	0.50
373	0.51
383	0.50
393	0.47
403	0.42
413	0.37

Another important parameter that can analyze the electrical response is the complex electric modulus $M^*(f)$. The dielectric relaxation processes of LNMO compound were examined through $M^*(f)$ that is described as [48-51]:

$$M^*(f) = M' + i\,M'' \qquad (6)$$

where M' and M'' are the real and imaginary components of the complex modulus, respectively. For more insights into the relaxation process, the frequency dependence of M' and M'' (Fig. 5 (a, b)) is very useful to understand such a process [52, 53]. As illustrated in Fig. 5(a), M' has a gradual increase with the increased frequency until reaches a peak value and then gets lowered at high frequencies. Such behavior is as S-sharp and attributed to an ionic conduction [54]. On the other hand, M'' curves (Fig. 5(b)) reveal relaxation peaks. This peak shifts toward higher frequencies as the applied temperature increases. The low-frequency part of M'' is associated with the charge carriers range within the carriers have a dynamic behavior over large distances [55].

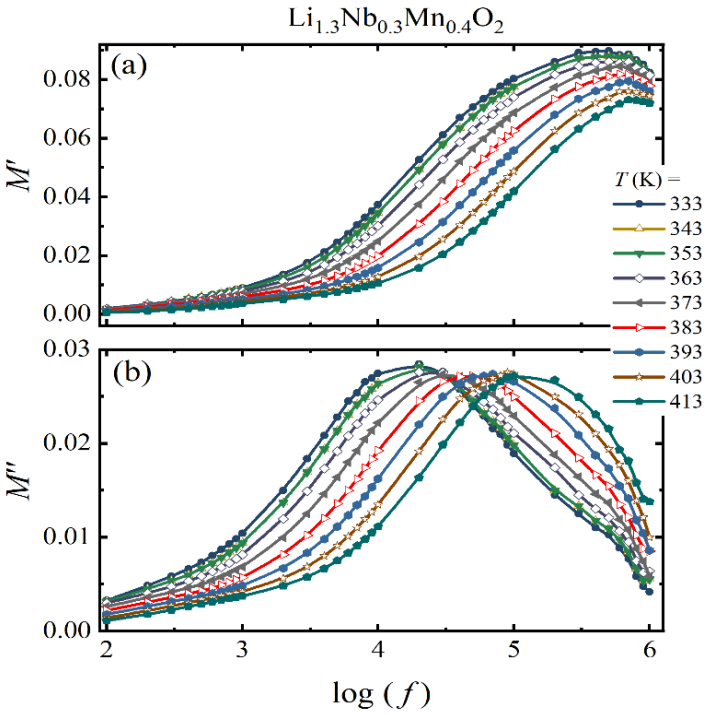

Fig. 5. The frequency dependence of (a) the real dielectric modulus (M'); (b) the imaginary dielectric modulus (M'') at different temperatures.

In the dielectric relaxation low-frequency side, the temperature dependence of the maximum frequency f_{max} is described as [55, 56]:

$$f_{max} = f_0 \, exp(-E_r/k_B T) \quad (7)$$

where f_0 is the pre-exponential term, and E_r is the relaxation activation energy. Fig. 6 depicts the temperature dependence of f_{max}, hence the relaxation energy was calculated from the data fitting to be 121 meV.

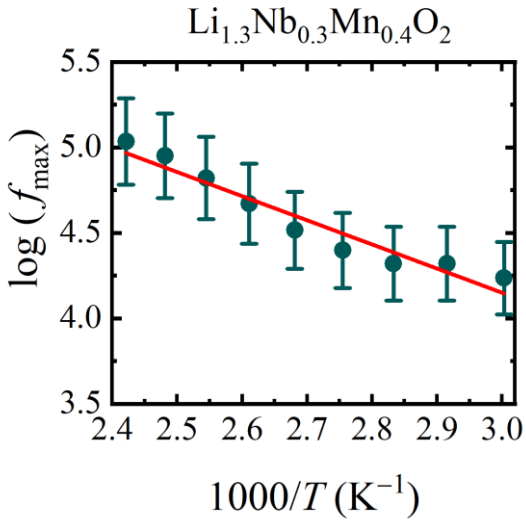

Fig. 6. The variation of log f_{max} versus 1000/T. The red line is the linear fitting according to Eq. 7.

Fig. 7. depicts normalized M''/M''_{max} against f/f_{max} that the normalized scaling behavior of LNMO is studied through this plot. It is noticed that the curves at different temperatures are overlapped. This is an indication that the dynamic process is temperature-independent [57]. Therefore, this is evidence of the presence of a relaxation process in the conductivity of LNMO [58]. Moreover, the frequency temperature superposition (FTS) principle is applied which also confirms the relaxation mechanism in LNMO sample [59].

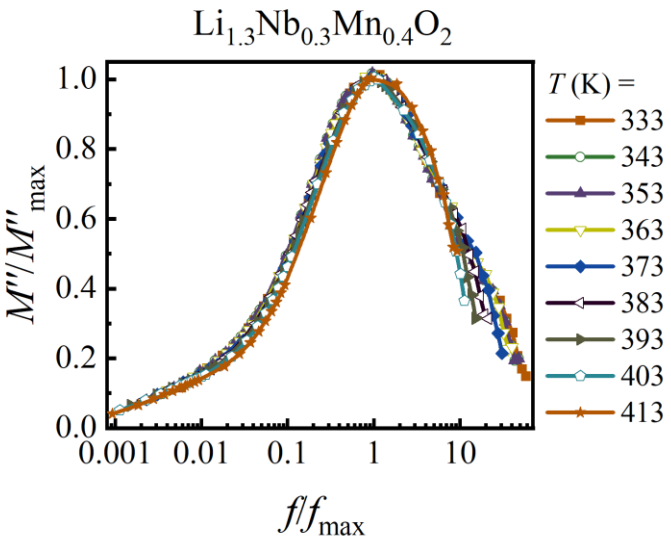

Fig. 7. Modulus master curve (M''/M''_{max} against f/f_{max}) at various temperatures.

Temperature dependence

Fig. 8(a-d) depicts the temperature dependence of ε' and ε'', tan δ and σ_{AC} at various frequencies. As seen, both ε' and ε'' are temperature-dependent at different frequencies. The behavior of tan δ versus temperature (Fig. 8 (c)) is similar to the variation of the ε'' (T). The change of σ_{AC} against $1000/T$ is represented in Fig. 8(d) at various frequencies. The σ_{AC} data were fitted in the temperature range from 363 to 414 K using Arrhenius relation [60]:

$$\sigma_{AC} = \sigma_0 \, exp(-E_a/k_B T) \quad (8)$$

where σ_0 is the pre-exponential factor, and E_a is the activation energy. The calculated E_a according to various frequencies is shown in Table 3.

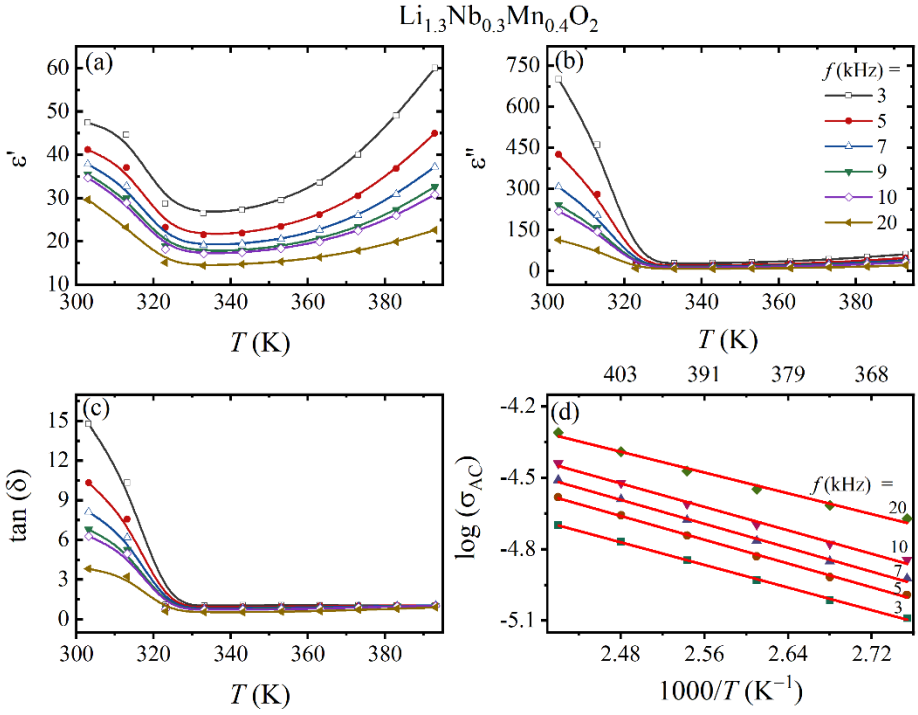

Fig. 8. The temperature dependence of (a) dielectric constant ε'; (b) dielectric loss ε''; (c) the loss factor (tan δ); (d) log σ_{AC} versus $1000/T$ and T at various frequencies. The red lines in (d) represent the fitting according to Eq. 8.

Table 3. The calculated activation energy (E_a) of LNMO at different frequencies.

f (kHz)	E_a (eV)
3	0.101
5	0.106
7	0.107
10	0.105
20	0.093

The temperature dependence of M' and M'' at various frequencies is illustrated in Fig. 9(a, b). In (Fig. 9(a)), M' shows a steady value beginning above room temperature up to $T \approx 353$ K and then decreases with increasing the temperature for all applied frequencies. Besides, the imaginary part M'' (Fig. 9(b)) has a higher starting value at low temperatures region and gets lowered as the temperature rises.

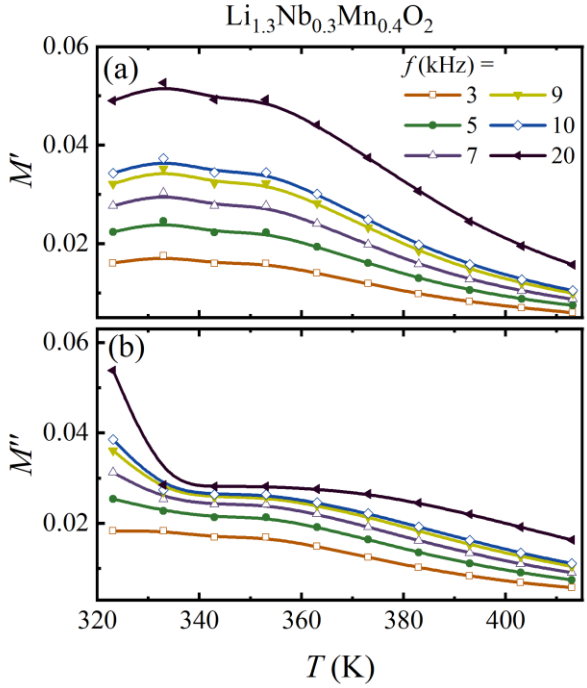

Fig. 9. The temperature dependence of (a) M'; (b) M'' at various frequencies.

4. Conclusions

From the FTIR spectrum, the compound showed symmetrical bending and stretching vibrations of Li-O and TM-O at the low wavenumber region. TGA results, the sample experienced two close weight losses, from 303 to 609 K and from 609 to 787 K. Besides, the DSC curve illustrates an endotherm peak at T = 1055 K with a reaction enthalpy (ΔH) = 306.78 J/g. This gives evidence for the thermal stability of the LNMO sample. The dielectric parameters ε', ε'' and tan δ are high at low frequencies because of the potential barrier generated by the space charge polarization at the grain boundaries. On the other hand, the conduction of LNMO is correlated barrier hopping (CBH) at $f \leq 1$ kHz and 363 K $\leq T \leq$ 413 K. Moreover, $\sigma_{AC}(T)$ is thermally activated with verification of the Ahrenious relation at $T > 363$ K. The activation energy (E_a) was calculated to be in the range of meV. From the imaginary part of complex modulus M'', there is a relaxation process that relies upon both frequency and temperature. Moreover, the relaxation activation energy (E_r) was calculated to be 121 meV. Overall, the reported results in this work would assist the previous studies concerning the applications of LNMO as a cathode material for Li-ion batteries.

Acknowledgment

The authors would like to thank Fayoum University for supporting the publication of this work.

Author Contributions

All authors contributed to this work. M. Kamel prepared the samples and completed the experimental measurements. Both A. Hassen and M. Abdel-Hafiez shared writing and followed the performance of the experiments. A. Hassan helped the first author complete the sample preparation. A. Hassen with M. Kamel completed the paper writing, analyzing the data, and validation. A. Hassen followed the revision and submission of the manuscript for publication.

Declaration of Competing Interest

The authors declare that they have no known competing financial interests or personal relationships that could have appeared to influence the work reported in this paper.

References

[1] L. Nie, S. Chen, W. Liu, Challenges and strategies of lithium-rich layered oxides for Li-ion batteries, Nano Res., 16 (2023) 391-402.
[2] H. Bashirpour-bonab, Experimental study and optimization of excess lithium in cathodic active materials with $Li_x(Ni_{0.3}Mn_{0.5}Co_{0.2})O_2$ composition on Li-ion battery performance, Int. J. Energy Res., 46 (2022) 7451-7459.
[3] J.B. Goodenough, K.-S. Park, The Li-Ion Rechargeable Battery: A Perspective, J. Am. Chem. Soc., 135 (2013) 1167-1176.
[4] D. Chen, J. Ahn, G. Chen, An Overview of Cation-Disordered Lithium-Excess Rocksalt Cathodes, ACS Energy Lett., 6 (2021) 1358-1376.
[5] W. Zhu, J. Zhang, J. Luo, C. Zeng, H. Su, J. Zhang, R. Liu, E. Hu, Y. Liu, W.-D. Liu, Y. Chen, W. Hu, Y. Xu, Ultrafast Non-Equilibrium Synthesis of Cathode Materials for Li-Ion Batteries, Adv. Mater., 35 (2023) 2208974.
[6] M.S. Whittingham, Lithium Batteries and Cathode Materials, Chem. Rev., 104 (2004) 4271-4302.
[7] B.L. Ellis, K.T. Lee, L.F. Nazar, Positive Electrode Materials for Li-Ion and Li-Batteries, Chem. Mater., 22 (2010) 691-714.
[8] M. Li, J. Lu, Z. Chen, K. Amine, 30 Years of Lithium-Ion Batteries, Adv. Mater., 30 (2018) 1800561.
[9] A. Manthiram, A reflection on lithium-ion battery cathode chemistry, Nat. Commun., 11 (2020) 1550.
[10] K. Turcheniuk, D. Bondarev, V. Singhal, G. Yushin, Ten years left to redesign lithium-ion batteries, Nature, 559 (2018) 467-470.
[11] D.-H. Kwon, J. Lee, N. Artrith, H. Kim, L. Wu, Z. Lun, Y. Tian, Y. Zhu, G. Ceder, The Impact of Surface Structure Transformations on the Performance of Li-Excess Cation-Disordered Rocksalt Cathodes, Cell Rep. Phys. Sci., 1 (2020) 100187.
[12] J. Lee, D.A. Kitchaev, D.H. Kwon, C.W. Lee, J.K. Papp, Y.S. Liu, Z. Lun, R.J. Clément, T. Shi, B.D. McCloskey, J. Guo, M. Balasubramanian, G. Ceder, Reversible Mn^{2+}/Mn^{4+} double redox in lithium-excess cathode materials, Nature, 556 (2018) 185–190.
[13] H. Zhang, X. Gao, Q. Cai, X. Zhang, Y. Tian, M. Jia, W. Xie, Y. Du, X. Yan, Recent Progress and Perspective of Cation Disordered Rock-salt Material for Advanced Li-ion Batteries, J. Mater. Chem. A, DOI 10.1039/D3TA00852E(2023).
[14] L. Huang, P. Zhong, Y. Ha, Z. Cai, Y.-W. Byeon, T.-Y. Huang, Y. Sun, F. Xie, H.-M. Hau, H. Kim, M. Balasubramanian, B.D. McCloskey, W. Yang, G. Ceder, Optimizing Li-Excess Cation-Disordered Rocksalt Cathode Design Through Partial Li Deficiency, Adv. Energy Mater., 13 (2023) 2202345.
[15] Z. Lun, B. Ouyang, Z. Cai, R.J. Clément, D.-H. Kwon, J. Huang, J.K. Papp, M. Balasubramanian, Y. Tian, B.D. McCloskey, H. Ji, H. Kim, D.A. Kitchaev, G. Ceder, Design Principles for High-Capacity Mn-Based Cation-Disordered Rocksalt Cathodes, Chem, 6 (2020) 153-168.
[16] J. Lee, X. Urban A Fau - Li, D. Li X Fau - Su, G. Su D Fau - Hautier, G. Hautier G Fau - Ceder, G. Ceder, Unlocking the potential of cation-disordered oxides for rechargeable lithium batteries, Science, 343 (2014) 519-522.
[17] A. Urban, A. Abdellahi, S. Dacek, N. Artrith, G. Ceder, Electronic-Structure Origin of Cation Disorder in Transition-Metal Oxides, Phys. Rev. Lett., 119 (2017) 176402.
[18] A. Urban, I. Matts, A. Abdellahi, G. Ceder, Computational design and preparation of cation-disordered oxides for high-energy-density Li-ion batteries, Adv. Energy Mater., 6 (2016) 1600488.
[19] N. Yabuuchi, M. Takeuchi, M. Nakayama, H. Shiiba, M. Ogawa, K. Nakayama, T. Ohta, D. Endo, T. Ozaki, T. Inamasu, K. Sato, S. Komaba, High-capacity electrode materials for rechargeable lithium batteries:Li_3NbO_4-based system with cation-disordered rocksalt structure, Proc. Natl. Acad. Sci. U.S.A., 112 (2015) 7650.
[20] M. Kamel, A.R.N. Hanna, C. Krellner, R. Klingeler, M. Abdellah, M. Abdel-Hafiez, A. Hassen, A.S.G. Khalil, T. Abdel-Baset, A. Hassan, Synthesis, Optical, Magnetic and Thermodynamic Properties of Rocksalt $Li_{1.3}Nb_{0.3}Mn_{0.4}O_2$ Cathode Material for Li-Ion Batteries, Crystals, 11 (2021) 825.
[21] Y. Huang, Y.-C. Lin, D.M. Jenkins, N.A. Chernova, Y. Chung, B. Radhakrishnan, I.-H. Chu, J. Fang, Q. Wang, F. Omenya, S.P. Ong, M.S. Whittingham, Thermal Stability and Reactivity of Cathode Materials for Li-Ion Batteries, ACS Appl. Mater. Interfaces, 8 (2016) 7013-7021.
[22] W.H. Kan, D. Chen, J.K. Papp, A.K. Shukla, A. Huq, C.M. Brown, B.D. McCloskey, G. Chen, Unravelling Solid-State Redox Chemistry in $Li_{1.3}Nb_{0.3}Mn_{0.4}O_2$ Single-Crystal Cathode Material, Chem. Mater., 30 (2018) 1655-1666.
[23] H.Y. Xu, H. Wang, Z.Q. Song, Y.W. Wang, H. Yan, M. Yoshimura, Novel chemical method for synthesis of LiV_3O_8 nanorods as cathode materials for lithium ion batteries, Electrochim. Acta, 49 (2004) 349-353.
[24] P. Suresh, S. Rodrigues, A.K. Shukla, H.N. Vasan, N. Munichandraiah, Synthesis of $LiCo_{1-x}Mn_xO_2$ from a low-temperature route and characterization as cathode materials in Li-ion cells, Solid State Ion., 176 (2005) 281-290.
[25] M. Rastgoo-Deylami, M. Javanbakht, H. Omidvar, Enhanced performance of layered $Li_{1.2}Mn_{0.54}Ni_{0.13}Co_{0.13}O_2$ cathode material in Li-ion batteries using nanoscale surface coating with fluorine-doped anatase TiO_2, Solid State Ion., 331 (2019) 74-88.
[26] S. Vinoth Rathan, G. Govindaraj, Thermal and electrical relaxation studies in $Li_{(4+x)}Ti_xNb_{1-x}P_3O_{12}$ ($0.0 \le x \le 1.0$) phosphate glasses, Solid State Sci., 12 (2010) 730-735.
[27] X. Bian, Q. Fu, X. Bie, P. Yang, H. Qiu, Q. Pang, G. Chen, F. Du, Y. Wei, Improved Electrochemical Performance and Thermal Stability of Li-excess $Li_{1.18}Co_{0.15}Ni_{0.15}Mn_{0.52}O_2$ Cathode Material by Li_3PO_4 Surface Coating, Electrochim. Acta, 174 (2015) 875-884.
[28] D. Ostrovskii, F. Ronci, B. Scrosati, P. Jacobsson, A FTIR and Raman study of spontaneous reactions occurring at the $LiNi_yCo_{(1-y)}O_2$ electrode/non-aqueous electrolyte interface, J. Power Sources, 94 (2001) 183-188.
[29] Q. Wu, X. Zhang, S. Sun, N. Wan, D. Pan, Y. Bai, H. Zhu, Y.-S. Hu, S. Dai, Improved electrochemical performance of spinel $LiMn_{1.5}Ni_{0.5}O_4$ through MgF_2 nano-coating, Nanoscale, 7 (2015) 15609-15617.
[30] L. Wang, Y. Zhan, S.-H. Luo, P. Li, Q. Wang, Y. Zhang, X. Liu, L. Chang, Two-position intrinsic element complement: Synthesis and electrochemical properties of $Li_{2+x}Mn_{1-x}SiO_4$@carbon as cathode materials for lithium batteries, Int. J. Energy Res., 45 (2021) 16922-16931.

[31] B. Vikram Babu, M. Sushma Reddi, K. Surendra, A. Rama Krishna, K. Samatha, V. Veeraiah, Synthesis, characterization and electrical studies of Nb-Substituted $Li_4Ti_5O_{12}$ anode materials for Li-ion batteries, Mater. Today: Proc., 43 (2021) 1485-1490.
[32] G. Siqin, Qilu, W. Tian, Scalable synthesis of high-voltage $LiNi_{0.5}Mn_{1.5}O_4$ with high electrochemical performances by a modified solid-state method for lithium ion batteries, Inorg. Chem. Commun., 134 (2021) 109067.
[33] C.R. Theocharis, C. Attipa, E. Hapeshi, A. Tillirou, R. Kokkinofta, Study of the Crystallization of Nanoporous Mixed Metal Oxide Phases, Adsorpt. Sci. Technol., 26 (2008) 643-650.
[34] L. Wang, T. Maxisch, G. Ceder, A First-Principles Approach to Studying the Thermal Stability of Oxide Cathode Materials, Chem. Mater., 19 (2007) 543-552.
[35] R. Gerhardt, Impedance and dielectric spectroscopy revisited: Distinguishing localized relaxation from long-range conductivity, J. Phys. Chem. Solids, 55 (1994) 1491-1506.
[36] M. Kamel, M. Abdel-Hafiez, A. Hassan, M. Abdellah, T.A. Abdel-Baset, A. Hassen, Optical, magnetic, thermodynamic, and dielectric studies of the disordered rock salt $Li_{1.3}Nb_{0.3}Fe_{0.4}O_2$ cathode for Li-ion batteries, J. Appl. Phys., 131 (2022) 155103.
[37] C. Rayssi, S. El.Kossi, J. Dhahri, K. Khirouni, Frequency and temperature-dependence of dielectric permittivity and electric modulus studies of the solid solution $Ca_{0.85}Er_{0.1}Ti_{1-x}Co_{4x/3}O_3$ ($0 \le x \le 0.1$), RSC Adv., 8 (2018) 17139-17150.
[38] I.S. Elashmawi, E.M. Abdelrazek, A.M. Hezma, A. Rajeh, Modification and development of electrical and magnetic properties of PVA/PEO incorporated with $MnCl_2$, Phys. B: Condens. Matter, 434 (2014) 57-63.
[39] B. Nageswara Rao, M. Venkateswarlu, N. Satyanarayana, Electrical and dielectric properties of rare earth oxides coated $LiCoO_2$ particles, Ionics, 20 (2014) 175-181.
[40] K. Yang, X. Huang, Y. Huang, L. Xie, P. Jiang, Fluoro-Polymer@$BaTiO_3$ Hybrid Nanoparticles Prepared via RAFT Polymerization: Toward Ferroelectric Polymer Nanocomposites with High Dielectric Constant and Low Dielectric Loss for Energy Storage Application, Chem. Mater., 25 (2013) 2327-2338.
[41] R. Singh, C. Maheshwaran, D.K. Kanchan, K. Mishra, P.K. Singh, D. Kumar, Ion-transport behavior in tetraethylene glycol dimethyl ether incorporated sodium ion conducting polymer gel electrolyte membranes intended for sodium battery application, J. Mol. Liq., 336 (2021) 116594.
[42] R. Jose, V. P, M.A. Rafiq, V.S. K, Investigation into defect chemistry and relaxation processes in niobium doped and undoped $SrBi_4Ti_4O_{15}$ using impedance spectroscopy, RSC Adv., 8 (2018) 34437-34448.
[43] A. Ladhar, M. Arous, H. Kaddami, M. Raihane, A. Kallel, M. Graça, L. Costa, AC and DC electrical conductivity in natural rubber/nanofibrillated cellulose nanocomposites, J. Mol. Liq., 209 (2015) 272-279.
[44] S.M. Soosen, A. Chandran, J. Koshy, K.C. George, Correlated barrier hopping in ZnO nanorods, J. Appl. Phys., 109 (2011) 113702.
[45] S. El-Sayed, K.H. Mahmoud, A.A. Fatah, A. Hassen, DSC, TGA and dielectric properties of carboxymethyl cellulose/polyvinyl alcohol blends, Phys. B: Condens. Matter, 406 (2011) 4068-4076.
[46] S. Karoui, H. Chouaib, S. Kamoun, Studies of electric, dielectric properties, and conduction mechanism of $\{(C_2H_{10}N_2)(MnCl(NCS)_2)_2\}_n$ polymer, J. Phys. Org. Chem., 33 (2020) e4101.
[47] M. Jebli, C. Rayssi, J. Dhahri, M. Ben Henda, H. Belmabrouk, A. Bajahzar, Structural and morphological studies, and temperature/frequency dependence of electrical conductivity of $Ba_{0.97}La_{0.02}Ti_{1-x}Nb_{4x/5}O_3$ perovskite ceramics, RSC Adv., 11 (2021) 23664-23678.
[48] Y. Badali, Ş. Altındal, İ. Uslu, Dielectric properties, electrical modulus and current transport mechanisms of Au/ZnO/n-Si structures, Prog. Nat. Sci.: Mater. Int., 28 (2018) 325-331.
[49] P. Sharma, D.K. Kanchan, M. Pant, K.P. Singh, Conductivity Studies in Proton Irradiated AgI-Ag_2O-V_2O_5-TeO_2 Super-Ionic Glass System, Mater. sci. appl., Vol.01No.02 (2010) 7.
[50] S. Ghosh, A. Ghosh, Electrical conductivity and conductivity relaxation in mixed alkali fluoride glasses, Solid State Ion., 149 (2002) 67-72.
[51] S.M. Suryawanshi, D.S. Badwaik, B.S. Shinde, K.D. Gaikwad, M. Shkir, K.V. Chandekar, S. Gundale, A comprehensive study on structural, magnetic and dielectric properties of $Ni_{0.3}Cu_{0.3}Zn_{0.4}Fe_{1.8}Cr_{0.2}O_4$ nanoparticles synthesized by sol-gel auto combustion route, J. Mol. Struct., 1272 (2023) 134173.
[52] M. Kaiser, Magnetic and electric modulus properties of In substituted Mg–Mn–Cu ferrites, Mater. Res. Bull., 73 (2016) 452-458.
[53] A. Rahal, S.M. Borchani, K. Guidara, M. Megdiche, Electrical, dielectric properties and study of AC electrical conduction mechanism of $Li_{0.9\square0.1}NiV_{0.5}P_{0.5}O_4$, R. Soc. Open Sci., 5 (2018) 171472.
[54] M.F. Mostafa, A. Hassen, Phase transition and electric properties of long chain Cd(II) layered perovskites, Ph. Transit., 79 (2006) 305-321.
[55] A. Dhahri, E. Dhahri, E. Hlil, Electrical conductivity and dielectric behaviour of nanocrystalline $La_{0.6}Gd_{0.1}Sr_{0.3}Mn_{0.75}Si_{0.25}O_3$, RSC Adv., 8 (2018) 9103-9111.
[56] S.M. Khan, M. Sharmin, M. Khan, A. Akther Hossain, M.D. Rahaman, Synthesis, structural, microstructural and electromagnetic properties of $(1-x)[Ni_{0.25}Cu_{0.15}Zn_{0.60}Fe_2O_4]+(x)[Na_{1/3}Ca_{1/3}Bi_{1/3}Cu_3Ti_4O_{12}]$ composites, Journal of Materials Science: Materials in Electronics, 30 (2019) 15388-15412.
[57] S. Saha, T. Sinha, Low-temperature scaling behavior of $BaFe_{0.5}Nb_{0.5}O_3$, Phys. Rev. B., 65 (2002) 134103.
[58] G.R. Gajula, L.R. Buddiga, K.N. Chidambara Kumar, M. Dasari, Study on electric modulus, complex modulus and conductivity properties of Nb/Sm, Gd doped barium titanate-lithium ferrite ceramic composites, Results Phys., 17 (2020) 103076.
[59] A. Abou Elfadl, S. El-Sayed, A. Hassen, A. El-Kader, G. Said, Charge transport and glassy dynamics in polyisoprene, Polym. Bull., 71 (2014) 2039-2052.
[60] M. Afifi, A. Bekheet, E. Abd Elwahhab, H. Atyia, Ac conductivity and dielectric properties of amorphous In_2Se_3 films, Vacuum, 61 (2001) 9-17.